

DRAFT VERSION JULY 18, 2025

Typeset using L^AT_EX **modern** style in AASTeX631

Solar Alfvénic Pulses and Mesoscale Solar Wind

JEONGWOO LEE,^{1,2,3} MANOLIS K. GEORGOULIS,^{4,5} RAHUL SHARMA,⁶
NOUR E. RAOUAFI,⁴ QIN LI,^{1,2,3} AND HAIMIN WANG^{1,2,3}

¹*Institute for Space Weather Sciences, New Jersey Institute of Technology, Newark, NJ 07102, USA*

²*Center for Solar-Terrestrial Research, New Jersey Institute of Technology, Newark, NJ 07102, USA*

³*Big Bear Solar Observatory, New Jersey Institute of Technology, Big Bear City, CA 92314, USA*

⁴*Johns Hopkins Applied Physics Laboratory, 11100 Johns Hopkins Road, Laurel, MD 20723, USA*

⁵*Research Center for Astronomy and Applied Mathematics, Academy of Athens, 11527 Athens, Greece (on leave)*

⁶*Department of Mathematics, Physics and Electrical Engineering, Northumbria University, Ellison Pl, Newcastle Upon Tyne, NE1 8ST, UK*

ABSTRACT

Large-scale solar ejections are well understood, but the extent to which small-scale solar features directly influence the solar wind remains an open question, primarily due to the challenges of tracing these small-scale ejections and their impact. Here, we measure the fine-scale motions of network bright points along a coronal hole boundary in high-resolution H α images from the 1.6m Goode Solar Telescope at Big Bear Solar Observatory to quantify the agitation of open flux tubes into generating Alfvénic pulses. We combine the motion, magnetic flux, and activity duration of the flux tubes to estimate the energy content carried by individual Alfvénic pulses, which is $\sim 10^{25}$ erg, adequately higher than the energies $\sim 10^{23}$ erg estimated for the magnetic switchbacks observed by the Parker Solar Probe (PSP). This implies the possibility that the surface-generated Alfvénic pulses could reach the solar wind with sufficient energy to generate switchbacks, even though some of them are expected to be reflected back in the stratified solar atmosphere. Alfvénic pulses further reproduce for the first time other properties of switchbacks, including the filling factor above $\sim 8\%$ at granular and supergranular scales, which correspond best to the lower end of the mesoscale structure. This quantitative result for solar energy output in the form of Alfvénic pulses through magnetic funnels provides a crucial clue to the ongoing debate about the dynamic cycle of energy exchange between the Sun and the mesoscale solar wind that has been raised, but has not been adequately addressed, by PSP near-Sun observations.

Keywords: Solar Alfvénic Pulses, mesoscale solarwind, magnetic switchbacks

1. INTRODUCTION

The question of how small-scale solar ejections may influence the inner heliosphere has always been timely since the prediction of solar wind (Parker 1958). The solar wind velocities measured by PSP as a function of helio-distance consist of numerous jets superimposed over a lower bound curve (Raouafi et al. 2023a). The latter curve seems to indicate the base solar wind obeying the Parker’s solar wind solution (Parker 1965), and the former suggests small-scale impulsive ejections from solar corona. The best visible and thus best known solar transients are coronal mass ejections (CMEs), which drive space weather (Howard et al. 2023). On the other hand, the smallest solar wind structure in the kinetic regime is probably formed en route without direct energy exchange with the Sun (Verscharen et al. 2019). Between them lies the so-called mesoscale regime with scales at 1 AU in the spatial range of 5–10,000 Mm and temporal range of 10 s to several hours, which must be important for the birth of the solar wind and the base of space weather (Viall et al. 2021). The Sun’s potential contribution to the mesoscale regime is the main focus of this study.

The Sun indeed has many features on the scales corresponding to the mesoscale, but it is hard to prove whether or not they can actually reach the heliosphere with sufficient energy and number, because of technical difficulties in tracking them from the Sun’s atmosphere to the solar wind. This said, the Parker Solar Probe (PSP; Raouafi et al. 2023b) flies sufficiently close to the Sun to amply detect a special feature called switchbacks, magnetic field deflections (Bale et al. 2019; Kasper et al. 2019; Dudok de Wit et al. 2020; Krasnoselskikh et al. 2020). Switchbacks are found in the MHD regime down to the ion gyroperiod (Dudok de Wit et al. 2020; Larosa et al. 2021; Viall et al. 2021; Shi et al. 2022; Choi et al. 2025) with the majority lying in the mesoscale (Figure 6 of Larosa et al. 2021). While identifying exclusive boundaries of the switchback scales needs further work on extracting pure switchback signals (e.g., Dudok de Wit et al. 2020), switchbacks are introduced as an important structure in the mesoscale (Viall et al. 2021). The solar features that we present in this study are in the MHD scale well below the CME scale, and thus, if found appropriate for the switchbacks, may provide a clue to the solar influence upon the mesoscale solar wind. The defining properties of switchbacks indicative of its solar origin include the modulation of groups of switchbacks at supergranulation scales and of individual features at granulation scales (Fargette et al. 2021; Bale et al. 2023, 2021; Lee et al. 2022), an aspect ratio and occurrence rate similar to that of spicules (Lee et al. 2022), and a base magnetic polarity distribution near coronal hole boundaries (Lee et al. 2024). Yet unexplored quantities such as the energy and filling factor of the Alfvénic pulses could also play a critical role, as these quantities measured in the Sun can be compared with those in the solar wind.

When searching for solar sources of solar wind transients, coronal hole boundaries are widely considered a key origin of switchback events (e.g., Bale et al. 2019; Rivera et al. 2024), where the photospheric magnetic field expands laterally and radially, establishing a direct connection between the solar surface and the interplanetary

magnetic field. This open magnetic topology lacks significant perpendicular inhomogeneities, thereby limiting interactions between outward-propagating wave pulses and the surrounding plasma. Under these conditions, nearly incompressible waves primarily undergo longitudinal–transverse mode coupling (Ulmschneider et al. 1991; Kalkofen 1997), which can gradually amplify wave amplitudes and lead to the development of large-amplitude Alfvénic waves, reported as potential switchback candidates (Rivera et al. 2024). A relationship has been suggested between the observed root-mean-square velocity amplitudes of transverse Alfvénic waves at different heights in the solar atmosphere and in the interplanetary medium (Wang & Sheeley 1990; Cranmer & van Ballegoijen 2005), by which the observed wave amplitudes can be scaled through expanding magnetic fields under the pressure balance between a magnetic flux tube and the surrounding atmosphere. The spatial scales of coherent Alfvénic waves observed in the corona (Sharma & Morton 2023) and those of switchback patches (Bale et al. 2019) are also comparable to supergranulation scales that could further be scaled down to measured wave energy injection scales in the photosphere (Abramenko et al. 2013) for uniformly expanding magnetic fields. This correspondence provides compelling evidence for a strong connection between the in-situ characteristics of switchbacks and their origins in the solar photosphere.

Recent PSP observations have further elucidated the processes of Alfvén waves as solar origin for switchbacks, including the distinction between solar surface-originating and in situ-generated mechanisms for Alfvénic switchback waves (Rivera et al. 2024), tracing switchbacks to the Sun using PSP’s perihelion encounters (Bowen et al. 2025; Bizien et al. 2025; Larosa et al. 2024) as well as simulating the generation of Alfvén waves in the Sun and their propagation into the solar wind (Wyper et al. 2024; Touresse et al. 2024). This increasing number of studies on Alfvén waves for switchbacks raise another timely question: under what conditions are Alfvénic pulses generated in the solar surface and are they strong enough to lead to switchbacks? In this Letter we study wave generation by directly measuring the fine-scale motion of the open field footpoints in the photosphere, under the premise –in lack of a definitive answer– that photospheric motions agitate field lines to excite Alfvén waves and that waves traveling along the open fields into space can possibly influence the mesoscale solar wind. Unlike previous studies investigating the wave origin of switchbacks (Squire et al. 2020; Shoda et al. 2021; Mallet et al. 2021; Squire et al. 2022; Johnston et al. 2022), we focus on the solar conditions required to generate Alfvénic waves with sufficient energy to produce the large deflections observed by PSP.

2. DATA

Essential in this study are high-resolution images and a powerful feature tracking tool. We use the high-resolution $H\alpha$ images obtained from the Visible Imaging Spectrometer (VIS; Cao et al. 2010) and magnetograms from Near-infrared Imaging Spectropolarimeter (NIRIS; Cao et al. 2012) mounted on the 1.6 m Goode Solar

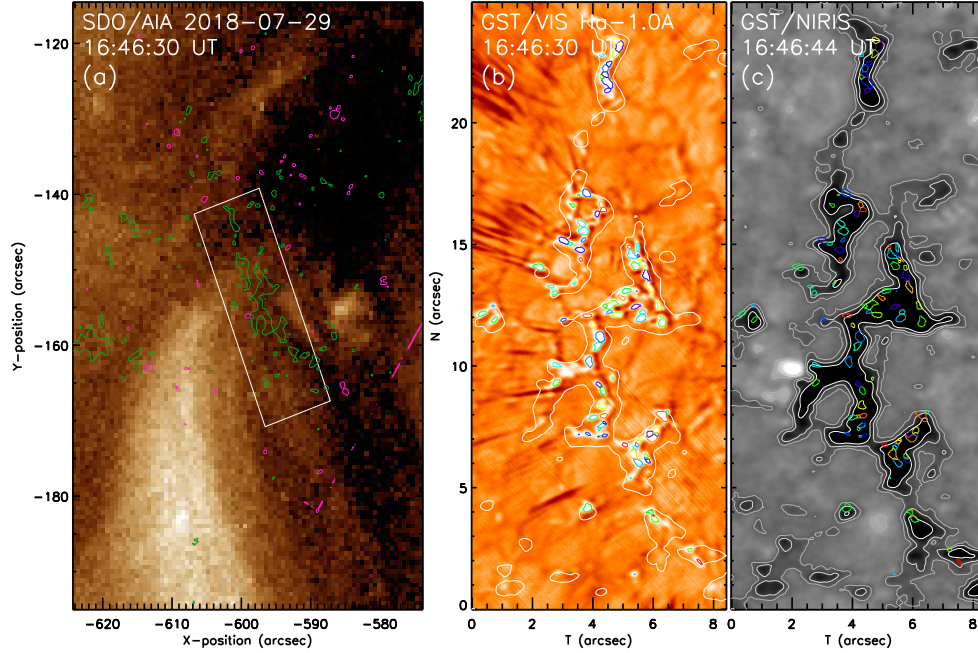


Figure 1. Target region in the coronal hole boundary. (a) SDO/AIA 193 Å image shows the coronal hole and EUV bright regions around. The superimposed contours represent the LoS magnetic field at +50 G (pink) and -50 G (green) from the NIRIS magnetogram. The white box denotes the FOV of the other panels. (b) H α far blue wing image in the sub-region shows spicules (dark straw-like features), filigree (white contours), and NBPs (crinkle-like features outlined by the colored contours). This field of view has the ordinate in the solar radius direction (named ‘N’) and the abscissa in the azimuthal direction (‘T’). (c) NIRIS LoS magnetogram as the gray background image and contours at $[-100, -50, -25, 25, 50]$ G. The NBPs (colored contours) appear only in single polarity fields. An animation (f1.mp4) is available showing this figure for the entire period of investigation from 16:31:40 UT to 18:06:59 UT.

Telescope (GST; Goode & Cao 2012) at Big Bear Solar Observatory (BBSO). The data were obtained on 2018 July 29 for a quiet-Sun coronal hole boundary region located about a half solar radius from the disk center at (604'' E, 125'' S). During this observation between 16:34–18:38 UT, NIRIS took high spatial resolution (0.24'') magnetograms and the VIS provided high resolution (0.10'') H α images at 11 wavelength points between $\pm 1\text{Å}$ in interval of 0.2 Å in the H α line center. The time interval between consecutive sets of the 11 wavelength point observation is 40 s. This cadence is adequate for the present analysis, because previous studies have reported the periodicity of transverse oscillations associated with MBPs in the range of 130–400 s (Jess et al. 2012; Berbery et al. 2024). From the coaligned NIRIS magnetograms one can then determine the line-of-sight (LoS) magnetic field or de-project it for an estimate of the vertical magnetic field, B_z (see also Figure 4).

Figure 1 shows a region of the chromospheric network near the coronal hole boundary, as can be identified with the SDO/AIA 193 Å image (Figure 1a). The fine structure of the network boundary is visible in the high resolution H α far wing image of GST/VIS (Figure 1b). The straw-like dark features are spicules (Secchi 1877) and

the bright lanes underneath spicules are filigree (Dunn & Zirker 1973). The filigree consisted of many crinkles called Network Bright Points (NBPs), also called Magnetic Bright Points (MBPs). The brightness is generally believed to result from a reduction in opacity when plasma escapes along open field lines (Dunn & Zirker 1973). The NIRIS magnetogram is shown in Figure 1c as a background grayscale image, and the overplotted colored polygons representing NBPs are taken from Figure 1b. It is notable that these NBPs lie within the unipolar magnetic fields concentrated along the coronal hole boundary (Figure 1c). NBPs move in network fields due to an evolving magneto-convection pattern (van Ballegooijen et al. 1998; Nisenson et al. 2003; Utz et al. 2010; Chitta et al. 2012), and this motion is believed to excite flux tube waves, which propagate up to the corona and even the solar wind (Cranmer & van Ballegooijen 2005; Cranmer & Winebarger 2019; Soler et al. 2019).

3. RESULTS

3.1. Dynamics of NBPs

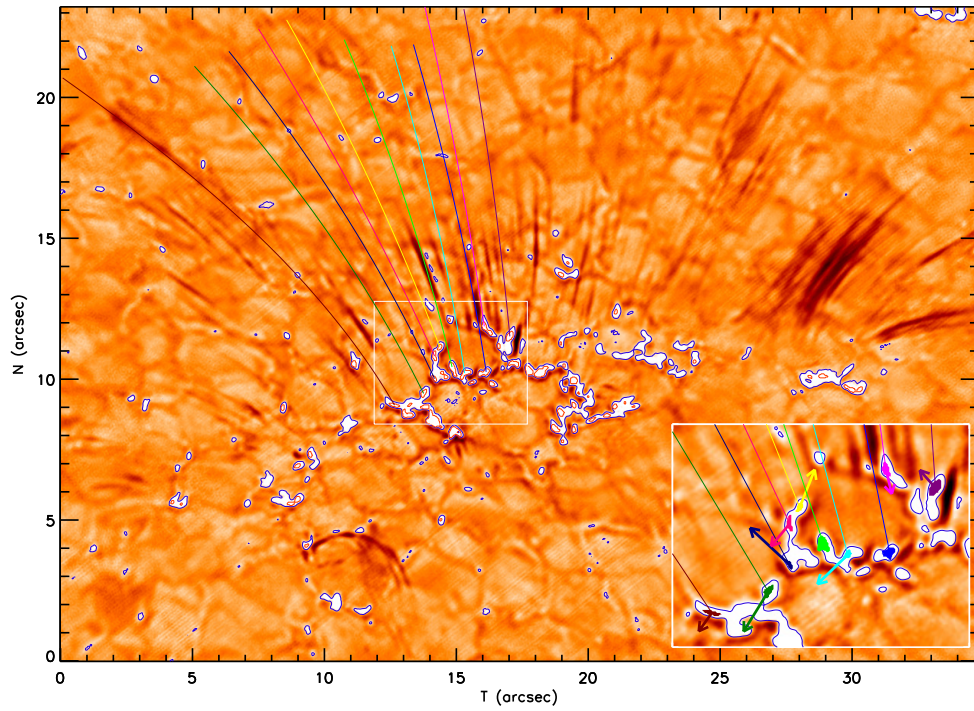


Figure 2. Spicules and NBPs in a GST/VIS $H\alpha$ -1.0Å blue wing image. A few field lines inferred from the selective spicule trajectories are marked in color together with NBPs outlined by a blue contour underneath. The inset magnifies the white box region, in which the color-filled masks represent the NBPs and associated field lines are colored in the same code. Using SWAMIS, we track each NBP in subsequent frames to determine its velocity (arrows in the inset).

Figure 2 shows spicules and NBPs over a $H\alpha$ blue wing image. Hypothetical field lines are set on the basis of the spicule trajectory and plotted to illustrate the open field lines. The inset shows the selected NBPs underneath the field lines. Their

random motions, as evident in the high-resolution $H\alpha$ movie, may agitate those field lines to generate Alfvén waves. In the solar atmosphere, Alfvén speed increases with height and the waves generated with a small amplitude in the photosphere will rapidly be amplified with height. Due to gradients in both density and magnetic field strength in the coronal hole boundary, Alfvénic fluctuations steepen, which may ultimately give rise to switchbacks (Shoda et al. 2021). The open field lines in this figure as a whole will then be able to reproduce a group of switchbacks on the size of a supergranule with the individual size of a granule (Fargette et al. 2021; Bale et al. 2021).

An important question here is not whether this motion can generate Alfvén waves, but whether these Alfvén waves carry the energy necessary to be detected by PSP if they manage to reach the PSP location. To answer this, a quantitative measurement of the subtle motions of NBPs is needed. We, however, found this challenging because many NBPs look alike and are closely seated. We use the Southwest Automatic Magnetic Identification Suite (SWAMIS; DeForest et al. 2007) for detection of NBPs in the VIS data, although it is an algorithm originally developed for tracking variable magnetic features near noise levels. SWAMIS first segments the filigrees and stores the results in “masks” such as the color-filled contours shown in the inset. Each mask is traced through subsequent frames, by which we can determine the motion and area of NBPs from their birth to death, and accordingly their lifetimes. Typical lifetimes of NBPs range from 40 s to a few min, close to the period of spicules (Okamoto & De Pontieu 2011), and therefore the waves generated are like pulses (Mackenzie Dover et al. 2021, 2022). They are generated by the transverse displacement of the flux tubes and can be identified as $m = 1$ kink mode waves, while Alfvén waves refer to a pure $m = 0$ mode with a strong torsional component (Mackenzie Dover et al. 2022). We hereafter call them Alfvénic pulses instead of Alfvén waves.

3.2. Feature Tracking

The top panel of Figure 3 shows NBP areas and motions determined using SWAMIS from the GST/VIS $H\alpha-1.0$ Å images. The feature recognition algorithm requires discrimination to separate the foreground features from the background noise. We define NBPs with the threshold for the $H\alpha$ intensity contrast, $(I - I_b)/I_b \geq 0.07$. As a result, NBPs have irregular shaped areas, which SWAMIS saves as masks (Figures 1 and 3). We represent each NBP by a circle at its center-of-mass position \mathbf{x}^k with an area A^k of the mask. By tracing \mathbf{x}^k of an NBP with the same ID number, k , in consecutive frames, we measure the displacement of the NBP and convert it to velocity using $\mathbf{u}^k = (\mathbf{x}^{k+1} - \mathbf{x}^k)/\Delta t$. Typical displacements of the NBPs from frame to frame ($\Delta t = 40$ s) are rather small, and we multiplied \mathbf{u}^k by a factor of 3 for better visibility. $(\mathbf{u}^k, \mathbf{x}^k)$ from the top panel are copied to the second panel, the GST/NIRIS magnetogram. Upon co-aligning the masked VIS pixels over simultaneous NIRIS magnetograms, two quantities are immediately available: the magnetic flux (cyan

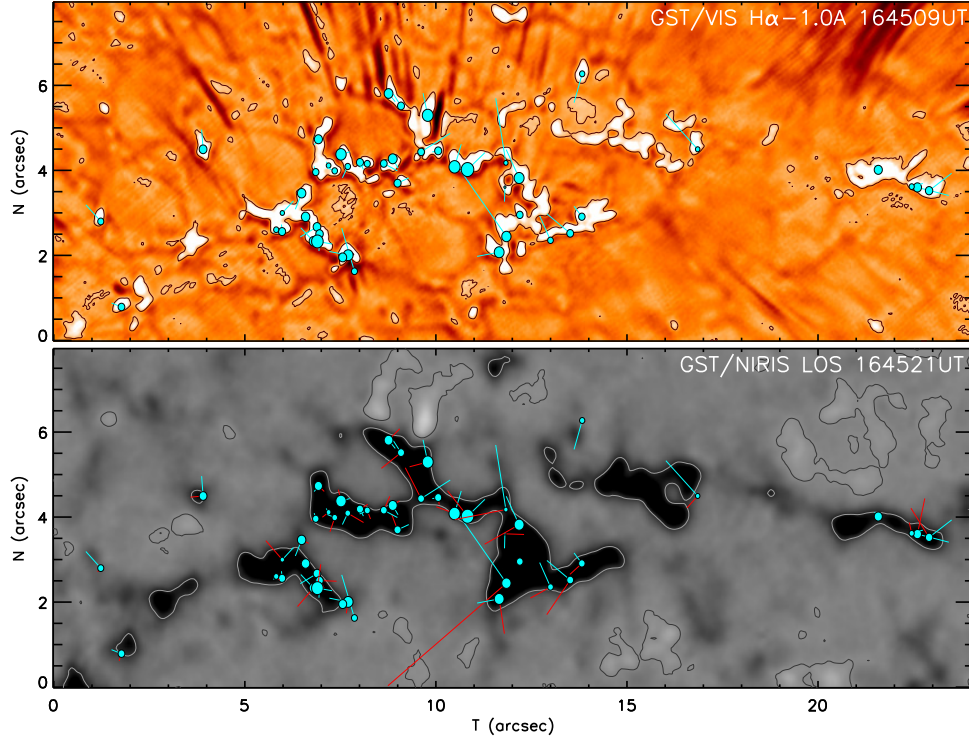


Figure 3. Tracking NBP motions in a magnetogram. In the top panel, NBPs are marked with cyan circles with equivalent area and their total displacements during their lifetimes are indicated by cyan lines (same in both plots), with length 3 times longer than actual displacements for visual convenience. The equivalent areas (cyan dots) and velocities (cyan lines) of these NBPs are further shown against the corresponding NIRIS LOS magnetogram, used to calculate the electric field vectors (red lines) shown in the bottom image.

dots) of the k -th NBP, $\phi_z^k = B_z^k A^k$ and the convective electric field $E_\perp^k = u^k B_z^k / c$ (red line) created by its motion (cyan line). The latter amounts to the transverse amplitude of the generated Alfvénic pulse. Note that we are measuring only the rectilinear motions of the NBPs to calculate the Alfvénic pulse energy. NBPs may show additional variations such as expansion, shrinkage, or deformation of their morphology. These motions may generate torsional Alfvén waves (Sharma & Morton 2023; Wedemeyer-Böhm et al. 2012), which we are unable to measure with the present data and technique.

3.3. Alfvénic Pulse Energy and Switchback Energy

We calculate the Alfvénic pulse energy on an individual basis by integrating the Alfvén wave flux over area and time:

$$\mathcal{E}_A \equiv \iint F \, da \, dt \quad \text{with} \quad F = \frac{1}{2} \rho u^2 V_A \quad (1)$$

For this energy to be useful for comparison with that of switchbacks under the wave origin hypothesis, the area integral $\int da$ should be over each fluxtube cross section, and time integral $\int dt$ over the lifetime of each driver, i.e., mobile NBPs. Figure

4a illustrates how we obtain these quantities from observations. The dotted line is the LoS, and the dashed lines are magnetic field lines that connect from the solar surface (a) to the solar wind (c). The angle, θ , represents the inclination of the local normal vector with respect to the LoS, and is $\approx 39^\circ$ from the disk location of this FOV. We divide the observed LoS component of the magnetic field by $\cos \theta$ to obtain local B_z , which is then used to calculate the two major quantities: magnetic flux of individual NBPs, $\phi_z = B_z A_z$, and the convective electric field $E_\perp = u B_z / c$ created by their motion, as displayed in Figure 3. The inclination of a field line is not used in this calculation, because we are using quantities perpendicular or parallel to the normal vector to the cross sectional area (denoted as A_z) of each flux tube lying on the photospheric surface. The NBP motion u_\perp is also confined to the surface and $\cos \theta$ is used to correct the projection effect.

With ϕ_z and E_\perp already calculated, we are left with the mass density ρ , the only quantity not directly obtained from this observation. For this purpose, we assume equipartition between the magnetic energy density and the ambient turbulent energy density, $\rho u^2 = B_z^2 / 4\pi$, so that the energy of an Alfvénic pulse is calculated by $\mathcal{E} = c\tau E_\perp \phi_z / 8\pi$, where τ is the duration of NBPs. We emphasize here that energy equipartition is regarded as suitable for active regions, i.e., kG fields (Georgoulis et al. 2012). However, the NBPs in the current study correlate with fields of a few hundred Gauss and are more mobile, so the ambient turbulence may be stronger than the magnetic field. In such environments, one expects a plasma $\beta > 1$, so assuming equipartition implies an underestimation of the density ρ and hence of the energy of Alfvénic pulses. As it stands, our analysis provides a lower limit of \mathcal{E} which is physically meaningful in our context.

It is desirable to calculate the amount of energy associated with magnetic reconnection as well. This requires additional information not only on NBPs but on their opposite polarity pairs and magnetic configuration. Although a more detailed study on this topic is underway (Georgoulis et al. 2025), we adopt a simplified assumption that all flux tubes attached to NBPs reconnect with their pairs and completely annihilate over a cylindrical volume with each side equal to the radius of the NBP. In this case, the magnetic energy to be released from an annihilation volume, πd^3 , is

$$\mathcal{E}_B \equiv \frac{B^2}{8} d^3. \quad (2)$$

In reality, neither all NBPs can reconnect with each other nor magnetic field inside an NBP would completely annihilate. This crude calculation is intended to give an upper bound for the magnetic energy available in the photosphere. Note that we use the same magnetic field and the fluxtube cross section, πd^2 , for both types of energy, and we should clarify what makes them different. As illustrated in Figure 3a, the magnetic energy is calculated by assuming the annihilation length of d . For the wave energy calculation, d is practically replaced by τV_A . The propagation speed V_A is

determined by the medium and τ by the driver so that τV_A may differ from d , and so does \mathcal{E}_A from \mathcal{E}_B .

Figure 4b shows the result of the above calculation. Since not all NBPs are alike, we plot their individual energies (orange area) as well as fluxes (blue bars) and electric fields (red bars) as number distributions. The magnetic flux of individual NBPs is distributed around a few 10^{17} Mx, one order of magnitude lower than the small-scale magnetic fluxes in the quiet Sun (Parnell 2002; Parnell et al. 2009). This makes sense because NBPs occupy a small fraction inside the network fields. The convective electric field E_\perp is around $0.1 - 1.0$ V cm $^{-1}$, which is about a hundred times smaller than the typical electric field associated with solar flares as estimated from flare ribbons (Lee 2022). Both the magnetic flux and the electric field are narrowly distributed, but they together make the wave energy in a broader distribution in the range of $10^{23} - 10^{26}$ erg with peak frequency of occurrence at 7×10^{24} erg.

To our knowledge this is the first time energies of individual Alfvénic wave pulse energies are calculated, whereas other studies typically calculate the energy flux density of Alfvénic pulses. Our estimate for the energy flux is around 5 kW m $^{-2}$ higher than reported elsewhere, for instance, $250-440$ W m $^{-2}$ (Okamoto & De Pontieu 2011; Wedemeyer-Böhm et al. 2012).

For the first time, we calculate the switchback energy using the simple scheme illustrated in Figure 4c. The N-shaped switchback is a schematic representation of a highly steepened Alfvénic pulse. The energy used to bend the fluxtube should be proportional to the increased length, ΔL . If the fluxtube has field strength B and area A , this energy is then expressed as $\Delta\mathcal{E} = B^2 \Delta L / 8\pi = \alpha B^2 D^3 / 32$ where D is diameter and $\alpha = L/D$ is the aspect ratio. We obtain these parameters for the six switchbacks listed in Table A.1 of Laker et al. (2021) and use them to find the magnetic energies in the range of $5 \times 10^{21} - 3 \times 10^{23}$ erg. The kinetic energy should be added to get the total energy of the switchbacks so that those plotted as red arrows in Figure 4d include a multiplicative factor of two. They are lower than the Alfvénic pulse’s energy $10^{23} - 10^{26}$ erg so that we can entertain a scenario that Alfvénic pulses impart their energy to switchbacks (Wedemeyer-Böhm et al. 2012). The magnetic energies are also shown as blue bars in Figure 4d, which lie in the range of $10^{19} - 10^{25}$ erg to overlap with the switchback energies (red arrows). If not all NBPs reconnect as we assume, then the actual number in each energy bin should reduce, albeit not the range of the energy distribution. If there were more numerous opposite-polarity patches in undetectably small sizes, the number in each energy bin would increase, but the dominant energy range can fall below that of switchbacks.

An unavoidable factor in the above energy comparison is the possible reflection of Alfvénic pulses in the solar atmosphere due to stratification of the density and magnetic field. On one hand, it makes the small amplitudes of the Alfvénic pulses in the photosphere rapidly increase with height, which can also lead to steepening of Alfvénic fluctuations, which could then create kinked structures such as switchbacks.

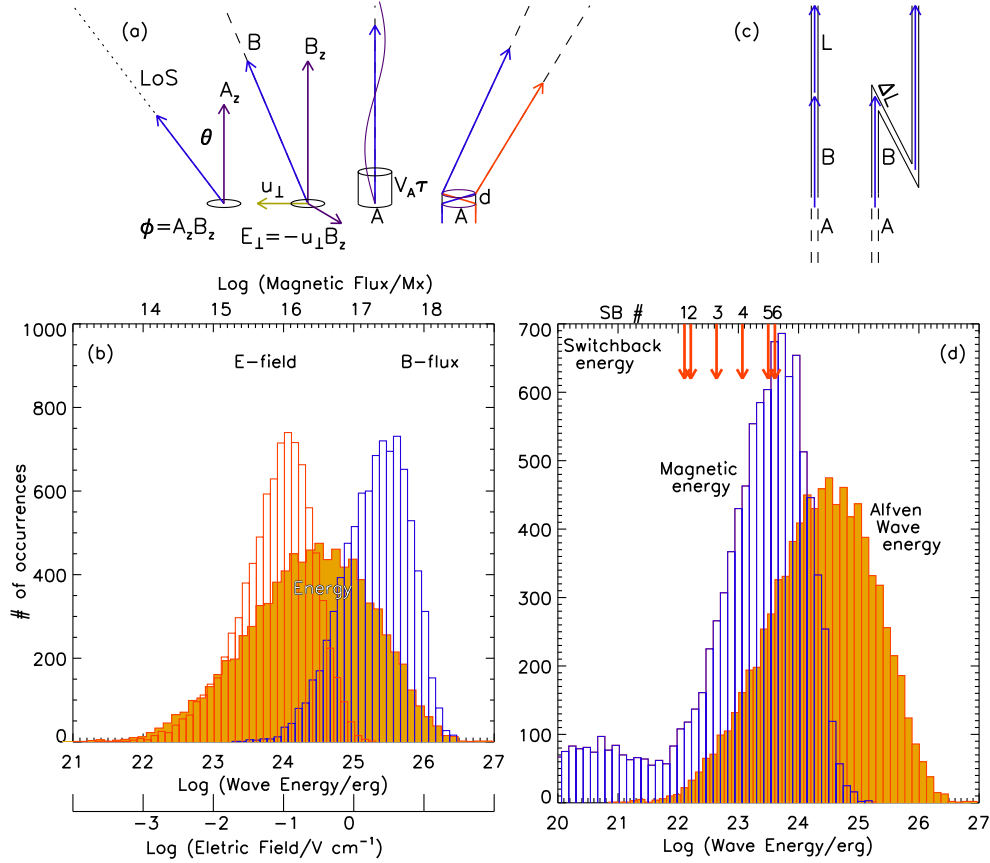


Figure 4. Illustration of the energy calculation and the associated parameters (top) and the distribution of the results. (a) Parameters in the photosphere and chromosphere. (b) Parameters of a magnetic switchback. (c) Number distributions of electric field, magnetic flux, and energy of Alfvénic pulses. (d) Energies of Alfvénic pulses (yellow) and those associated with magnetic reconnection (blue) in comparison with six switchback energies (red arrows). SB#1–6 refer to the PSP switchbacks with ID: E2S4, E2S6, E1S5, E1S6, E1S1, and E2S3 defined in [Laker et al. \(2021\)](#).

On the other hand, the corresponding change in Alfvén speed can cause reflection of Alfvénic pulses, especially at the transition layer ([Hollweg 1978](#); [Schwartz & Bel 1984](#); [Cranmer & van Ballegooijen 2005](#); [Chae & Lee 2023](#)). We calculated the reflection coefficient in Appendix A to find that 1–10% of the Alfvénic pulse energy can be transmitted through the transition region. This means that the range of transmitted energy will then shift down by one or two octaves with their number maintained. This energy distribution still overlaps with the energies of the switchbacks.

3.4. Spatial Distribution and Filling Factor of Alfvénic Pulses

Although the magnitudes of the flux ϕ_z , convective electric field E_\perp and energy \mathcal{E} of Alfvénic pulses are the ultimate goal of this study, their discrete spatial distribution and subsequent filling factor are also of interest for comparison with switchbacks measured in the form of time series. To visualize the spatial distribution of these quantities, we represent them as Gaussians centered at the position of each individual

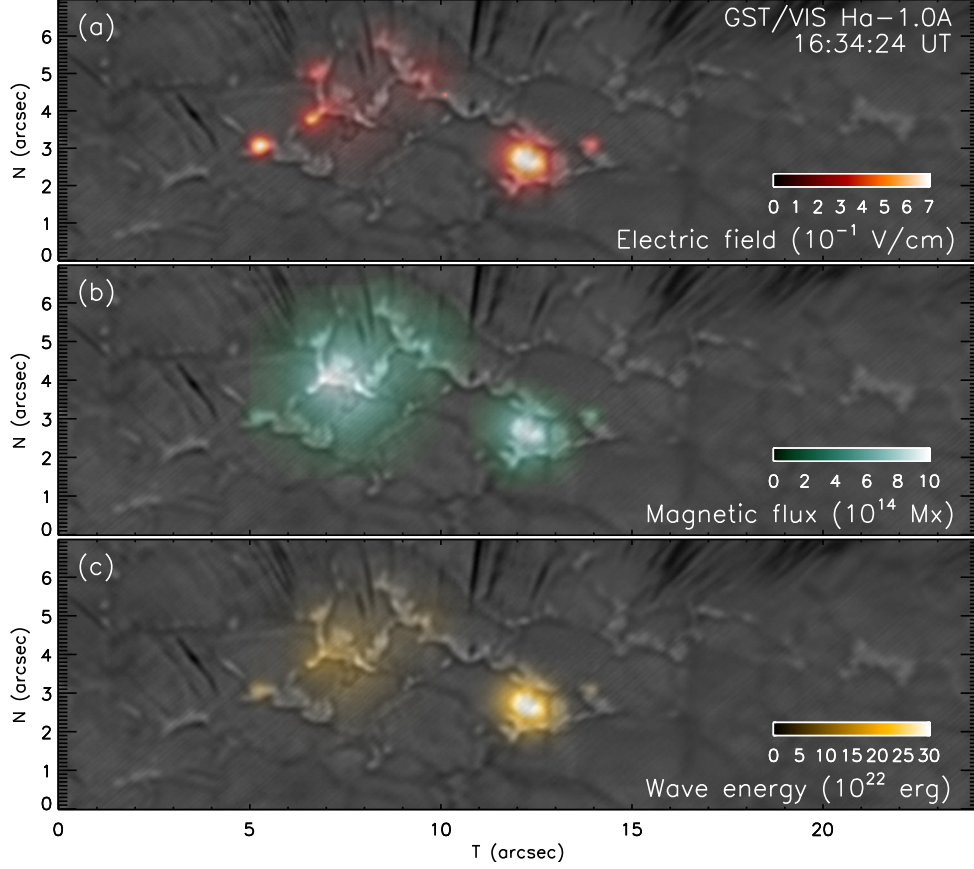


Figure 5. Physical quantities derived from the GST/VIS H α blue wing images and the GST/NIRIS magnetograms. (a) Convective electric field, (b) magnetic flux of NBPs, and (c) energy of Alfvénic pulses are plotted as color shades of Gaussians centered on individual NBPs. An animation (f5.mp4) of this figure is available for the period from 16:31:42 UT to 18:06:03 UT with the logarithmic scale bars instead of the linear scale bars as shown here.

NBP, wide in proportion to the diameter of the NBP and high in proportion to the magnitude of the quantities and plot them as colored shades over the H α far-wing image in Figure 5. The Gaussian assumption is only for visualization and does not affect the calculation made in the previous section. The magnetic fluxes of the NBPs (Figure 5b) and the energies of individual pulses (Figure 5c) are plotted in the same format. Comparison of the three panels in Figure 5 reveals that regions with the strongest electric field or magnetic flux are not necessarily the sites of the highest energy because mobile NBPs and strong field regions do not necessarily move in tandem. In general, NBPs moving in strong field regions produce intense electric field, while those in weak field region do not. Accordingly strong wave sources are more limited than NBPs themselves. In the accompanying animation, each frame shows a scale bar for the magnitude range of the plotted quantity, meant to show its variation in time.

The filling factor of NBPs, namely, how densely NBPs cover the solar surface, is another important constraint in the current Alfvén wave/turbulence models (Squire et al. 2020, 2022; Mallet et al. 2021; Shoda et al. 2021; Johnston et al. 2022). PSP

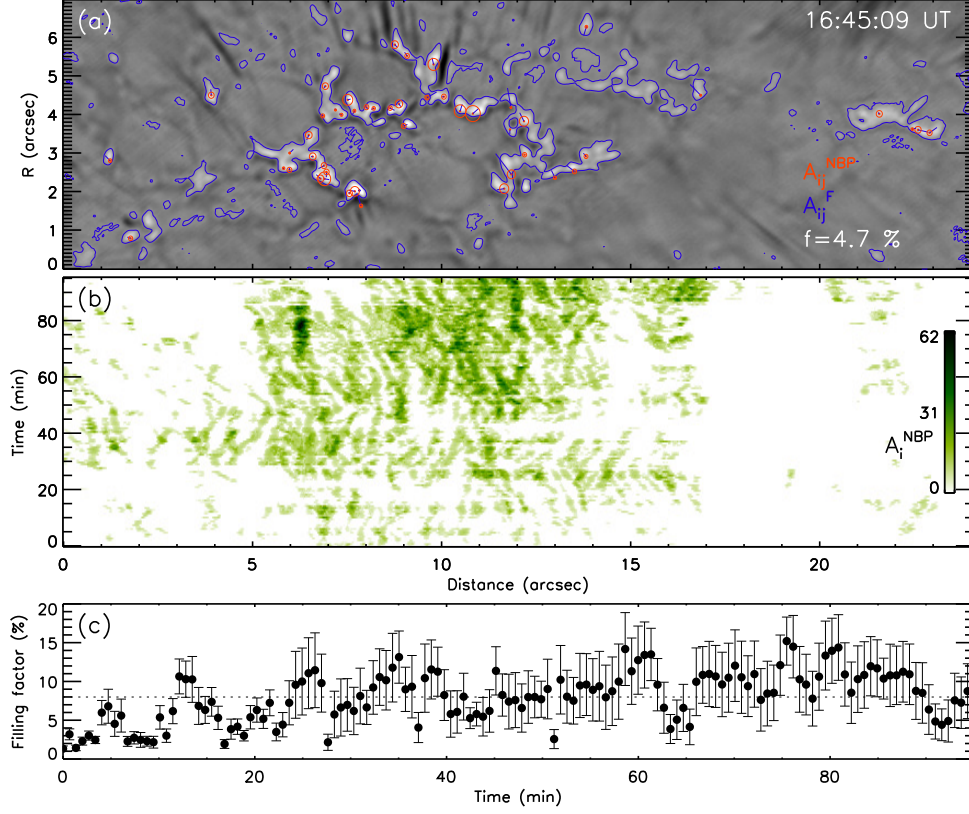


Figure 6. Filling factor of NBPs. (a) The areas of mobile NBPs (red circles) and filigree (blue contours). The filling factor is calculated by dividing the sum of the NBP areas by the total area of the filigree at each time. (b) Time-distance (T-R) map of the NBPs. At each time, the NBP areas along the T -axis is obtained by adding up the NBPs along the R -axis. (c) Average filling factor as a function of time. The error bars are based on the uncertainty in the filigree area and the dashed line at $\sim 8\%$ is the mean value of the filling factor over time.

observations show a filling factor as high as 6% (Bale et al. 2019), which is not well understood. We can reevaluate this parameter more carefully using the SWAMIS result. In Figure 6a, we mark the areas of mobile NBPs with red circles with equivalent areas in which by $A_{ij}^{NBP} = 1$ and zero otherwise, where i and j denote the pixel indices along the x - and y -axes, respectively. All filigree structures—including both mobile and immobile NBPs—are outlined with blue contours, inside which $A_{ij}^F = 1$ and zero outside. The latter represents the open field region which forms the solar wind with and without switchbacks. Under the current hypothesis, the field lines stemming from pixels with $A_{ij}^{NBP} = 1$ develop into switchbacks, and those from $A_{ij}^F = 1$ remain as straight field lines forming quiescent non-switchback regions in the solar wind. Therefore, the ratio of the total area of the mobile NBPs to that of the filigree:

$$f \equiv \frac{\sum_{i,j} A_{ij}^{NBP}}{\sum_{i,j} A_{ij}^F}. \quad (3)$$

should give the filling factor.

A single filling factor is obtained per image, with the positional information integrated out. To show the spatio-temporal distribution of NBPs, we calculate $A_i^{NBP} = \sum_j A_{ij}^{NBP}$ on each frame and stack them along the y-axis. Such 1-D structure along the T -axis is calculated over all 142 frames and stacked together to build the time-distance map in Figure 6b with the color set to be darker for larger values. The average filling factor is finally calculated by performing the summation over the T -axis as well and shown in Figure 6c as a function of time. The vertical error bars are based on the 2–3% intensity contrast threshold for defining the filigree region. The time-averaged filling factor is now as high as 8%, comparable to 6% of the switchbacks detected by PSP (Bale et al. 2019). Our high filling factor is obtained by excluding the regions considered irrelevant for comparison with switchbacks; they are either the field-free regions or the closed-field regions. The low filling factor predicted by Alfvén wave/turbulence models for switchbacks (Shoda et al. 2021) could also arise in this case if such solar surface conditions were not accounted for.

4. DISCUSSION

Using high-resolution H α images and magnetograms from BBSO/GST, we have investigated whether the Sun can generate Alfvénic pulses (Asgari-Targhi et al. 2013) strong enough to contribute to the meso-scale solar wind. Our results support the Alfvén wave/turbulence models for switchbacks (Squire et al. 2020, 2022; Mallet et al. 2021; Shoda et al. 2021; Johnston et al. 2022), but draw more attention to the solar source properties. The investigated solar wind source is located in the edge of a coronal hole, where steep gradients in both density and magnetic field can result in the steepening of Alfvénic fluctuations (Wang & Sheeley 1990) and thus shock-like structures characterized by high velocities and abrupt changes in magnetic field strength (Mackenzie Dover et al. 2022, 2021), favorable for the switchback formation. In these regions, the open magnetic fields are mainly unipolar, so that Alfvénic deflections propagating along them may be detected as a series of switchback-like structures by a flying spacecraft (Lee et al. 2022, 2024). Counting the discrete NBPs yields another important clue, the filling factor of Alfvénic pulses $\sim 8\%$ as high as detected by PSP measurements for the switchback patches (Bale et al. 2019). These solar properties, not fully adopted by in situ only modeling Shoda et al. (2021), augment the Alfvén wave/turbulence models for switchbacks (Squire et al. 2020, 2022; Mallet et al. 2021; Shoda et al. 2021; Johnston et al. 2022).

As a crucial step, we evaluated the potential solar candidates for switchbacks on an individual energy basis. Collection of tiny bipolar flux cancellations and the eruption of minifilaments may also contribute to the solar wind, but in smaller and larger individual energies, respectively. The energy of individual Alfvénic pulses lies in the range of $10^{24} - 10^{25}$ erg at generation (§2.3), but only a fraction of it will reach the solar wind due to strong reflection at the solar transition region. We estimated the transmission coefficient as 1–10% using parameters (§2.4), and expect the energy content

of the Alfvénic pulses in space is yet comparable to the energy range of switchbacks, $10^{22} - 10^{23}$ erg. The individual Alfvénic pulse energy and the overall filling factor (§2.5) serve as major quantities in connecting the Sun to switchbacks. While this study favors Alfvénic pulses as the solar source of the switchbacks, magnetic reconnection is also a strong candidate, if not primarily for switchbacks, but as a significant contributor to the bulk energy flux for powering the solar wind.

Since flux tubes kinked as sharply as switchbacks are rarely found in the Sun, the switchback morphology must form en route (Akhavan-Tafti & Soni 2024) and the Sun provides only seeds for switchbacks. In this case, we must consider how the Sun generates the seeds at the appropriate scale and rate for in situ switchback formation. The Sun as a star has the granular and supergranular structures that form under superadiabaticity in sizes determined by partial ionization of hydrogen and helium (Stix 2004). As flux tubes congregate toward the convective cell boundary and are enhanced there playing a role as generators and also conduits for the Alfvén waves (Simon & Leighton 1964; Cranmer & van Ballegoijen 2005), it is an inevitable consequence that modulations in those two convective scales are found in switchbacks (Bale et al. 2021; Fargette et al. 2021). It is then solar convection that underlies solar input to the meso-scale solar wind. An emerging picture is that the Sun outputs a granule-scale excess energy into the space utilizing Alfvénicity rather than direct mass transfer and the solar wind stores those small-scale excess energies in the form of magnetic switchbacks (Lee et al. 2024).

Switchbacks themselves seem to be able to heat and accelerate the solar wind non-adiabatically (Rivera et al. 2024), and further create disturbances, e.g., whistler waves, which can scatter strahl particles to regulate heat flux from the Sun (Cattell et al. 2022; Choi et al. 2024). This forms an important cycle of energy exchange between the Sun and the mesoscale solar wind. Together with the large-scale CMEs from strong fields accumulated in active regions (Zirin 1988), short-period Alfvénic pulses generated at the network boundary should complement the wide range of lower corona inputs to the solar wind.

We thank Drs Kyungeun Choi, Thierry Dudok de Wit, and Andrea Larosa for helpful discussions. This work was supported by NSF grants, AGS-2114201, AGS-2229064 and AGS-2309939, and NASA grants, 80NSSC19K0257, 80NSSC20K0025, 80NSSC20K1282 and 80NSSC24K0258. RS is grateful for support from the UKRI Future Leader Fellowship (RiPSAWMR/T019891/1).

Facilities: Big Bear Observatory (GST/VIS and GST/NIRIS)

Software: IDL, SolarSoft (Freeland & Handy 2012), SWAMIS (DeForest et al. 2007)

APPENDIX

A. REFLECTION OF ALFVÉNIC PULSES

The amount of wave energy that can be transmitted to the corona and the solar wind depends on the gradient of Alfvén speed and the wave frequency. Alfvénic pulses with frequencies higher than the critical frequency determined by the gradient of the Alfvén speed, $\omega_c = |\partial V_A / \partial z|/2$, can propagate as if in a homogeneous medium, while those with lower frequencies suffer reflection (Schwartz & Bel 1984). For a typical transition layer, ω_c^{-1} is about 10 s. In this case, the typical period of Alfvénic pulses of current interest is ~ 40 s (Okamoto & De Pontieu 2011), and significant reflection of them is expected. We calculated the transmission coefficient using a classical model (Zhugzhda & Locans 1982), which approximates the stratified solar atmosphere by a linear variation of temperature and an exponential variation of density. The transmission coefficient decreases with increasing Alfvén speed contrast, $\alpha = V_{A2}/V_{A1}$, across the transition layer, and also with decreasing density scale height, H_ρ . Figure 7 shows the calculated transmission coefficients. In the left panel, the transmission reduces with increasing Alfvén speed contrast, $\alpha = V_{A2}/V_{A1}$, across the transition layer, and also with decreasing density scale height, H_ρ . The right panel shows more systematically how the transmission coefficient depends on α and H_ρ at a fixed period. For a given H_ρ , lowering α increases the transmission coefficient. At a given α , a larger H_ρ allows better transmission of waves, because it effectively increases ω/ω_c . For plausible ranges of $10 \leq \alpha \leq 40$ and $200 \leq H_\rho \leq 400$ km, we can expect transmission of Alfvénic pulses through the transition layer as high as 1–10%, which is compatible with previous studies (Schwartz & Bel 1984; Cranmer & van Ballegoijen 2005; Chae & Lee 2023).

REFERENCES

- Abramenko, V. I., Zank, G. P., Dosch, A., et al. 2013, *ApJ*, 773, 167, doi: [10.1088/0004-637X/773/2/167](https://doi.org/10.1088/0004-637X/773/2/167)
- Akhavan-Tafti, M., & Soni, S. L. 2024, *ApJL*, 970, L26, doi: [10.3847/2041-8213/ad60bc](https://doi.org/10.3847/2041-8213/ad60bc)
- Asgari-Targhi, M., van Ballegoijen, A. A., Cranmer, S. R., & DeLuca, E. E. 2013, *ApJ*, 773, 111, doi: [10.1088/0004-637X/773/2/111](https://doi.org/10.1088/0004-637X/773/2/111)
- Bale, S. D., Badman, S. T., Bonnell, J. W., et al. 2019, *Nature*, 576, 237, doi: [10.1038/s41586-019-1818-7](https://doi.org/10.1038/s41586-019-1818-7)
- Bale, S. D., Horbury, T. S., Velli, M., et al. 2021, *ApJ*, 923, 174, doi: [10.3847/1538-4357/ac2d8c](https://doi.org/10.3847/1538-4357/ac2d8c)
- Bale, S. D., Drake, J. F., McManus, M. D., et al. 2023, *Nature*, 618, 252, doi: [10.1038/s41586-023-05955-3](https://doi.org/10.1038/s41586-023-05955-3)
- Berbery, A., Keys, P. H., Jess, D. B., & Christian, D. J. 2024, *A&A*, 690, A363, doi: [10.1051/0004-6361/202451199](https://doi.org/10.1051/0004-6361/202451199)
- Bizien, N., Froment, C., Madjarska, M. S., Dudok de Wit, T., & Velli, M. 2025, *A&A*, 694, A181, doi: [10.1051/0004-6361/202452140](https://doi.org/10.1051/0004-6361/202452140)
- Bowen, T. A., Mallet, A., Dunn, C. I., et al. 2025, arXiv e-prints, arXiv:2504.13384, doi: [10.48550/arXiv.2504.13384](https://doi.org/10.48550/arXiv.2504.13384)

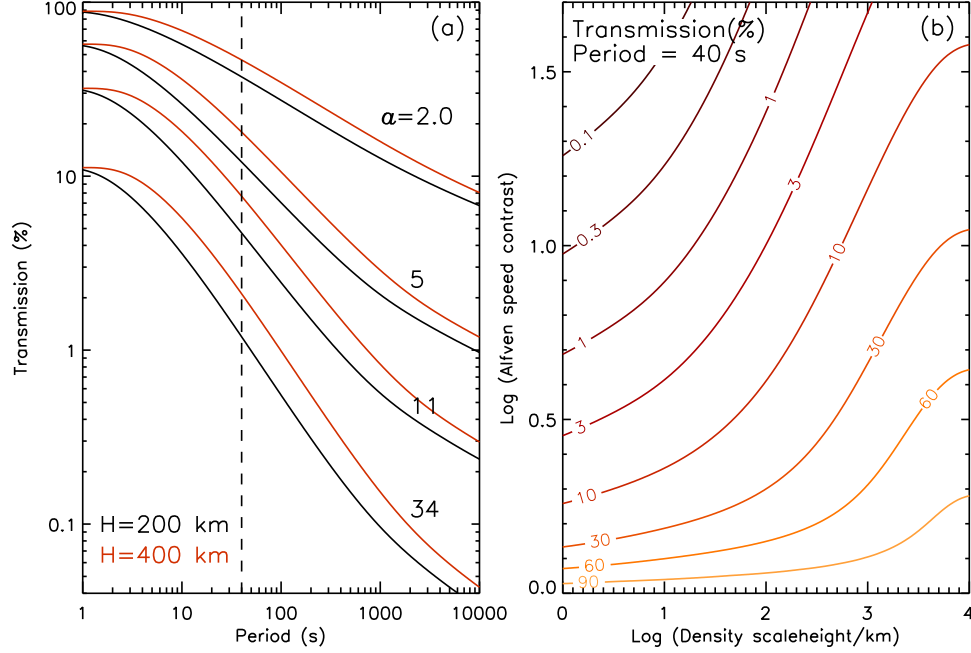


Figure 7. Transmission of Alfvénic pulses. (a) Transmission coefficient in energy as a function of period for selected values of the Alfvén speed contrast, $\alpha = V_{A2}/V_{A1}$ calculated for two density scale heights, H_ρ . (b) Transmission coefficient as a function of H_ρ and α at a fixed period of 40 s. Different contours between 0.1% and 90% are labeled with these percentage values. Darker contours denote stronger wave reflection.

- Cao, W., Goode, P. R., Ahn, K., et al. 2012, in *Astronomical Society of the Pacific Conference Series*, Vol. 463, Second ATST-EAST Meeting: Magnetic Fields from the Photosphere to the Corona., ed. T. R. Rimmele, A. Tritschler, F. Wöger, M. Collados Vera, H. Socas-Navarro, R. Schlichenmaier, M. Carlsson, T. Berger, A. Cadavid, P. R. Gilbert, P. R. Goode, & M. Knölker, 291. <https://ui.adsabs.harvard.edu/abs/2012ASPC..463..291C>
- Cao, W., Gorceix, N., Coulter, R., et al. 2010, *Astronomische Nachrichten*, 331, 636, doi: [10.1002/asna.201011390](https://doi.org/10.1002/asna.201011390)
- Cattell, C., Breneman, A., Dombeck, J., et al. 2022, *ApJL*, 924, L33, doi: [10.3847/2041-8213/ac4015](https://doi.org/10.3847/2041-8213/ac4015)
- Chae, J., & Lee, K.-S. 2023, *ApJ*, 954, 45, doi: [10.3847/1538-4357/ace771](https://doi.org/10.3847/1538-4357/ace771)
- Chitta, L. P., van Ballegoijen, A. A., Rouppe van der Voort, L., DeLuca, E. E., & Kariyappa, R. 2012, *ApJ*, 752, 48, doi: [10.1088/0004-637X/752/1/48](https://doi.org/10.1088/0004-637X/752/1/48)
- Choi, K.-E., Agapitov, O., Colombari, L., et al. 2024, *ApJ*, 971, 177, doi: [10.3847/1538-4357/ad54c4](https://doi.org/10.3847/1538-4357/ad54c4)
- Choi, K.-E., Agapitov, O. V., Lee, D.-Y., et al. 2025, *ApJ*, arXiv:2506.08278, doi: [10.48550/arXiv.2506.08278](https://doi.org/10.48550/arXiv.2506.08278)
- Cranmer, S. R., & van Ballegoijen, A. A. 2005, *ApJS*, 156, 265, doi: [10.1086/426507](https://doi.org/10.1086/426507)
- Cranmer, S. R., & Winebarger, A. R. 2019, *ARA&A*, 57, 157, doi: [10.1146/annurev-astro-091918-104416](https://doi.org/10.1146/annurev-astro-091918-104416)
- DeForest, C. E., Hagenaar, H. J., Lamb, D. A., Parnell, C. E., & Welsch, B. T. 2007, *ApJ*, 666, 576, doi: [10.1086/518994](https://doi.org/10.1086/518994)
- Dudok de Wit, T., Krasnoselskikh, V. V., Bale, S. D., et al. 2020, *ApJS*, 246, 39, doi: [10.3847/1538-4365/ab5853](https://doi.org/10.3847/1538-4365/ab5853)
- Dunn, R. B., & Zirker, J. B. 1973, *SoPh*, 33, 281, doi: [10.1007/BF00152419](https://doi.org/10.1007/BF00152419)
- Fargette, N., Lavraud, B., Rouillard, A. P., et al. 2021, *ApJ*, 919, 96, doi: [10.3847/1538-4357/ac1112](https://doi.org/10.3847/1538-4357/ac1112)

- Freeland, S. L., & Handy, B. N. 2012, SolarSoft: Programming and data analysis environment for solar physics, Astrophysics Source Code Library, record ascl:1208.013
- Georgoulis, M. K., Li, Q., Lee, J., Wang, H., & Raouafi, N. 2025, ApJ, in preparation
- Georgoulis, M. K., Titov, V. S., & Mikić, Z. 2012, ApJ, 761, 61, doi: [10.1088/0004-637X/761/1/61](https://doi.org/10.1088/0004-637X/761/1/61)
- Goode, P. R., & Cao, W. 2012, in Society of Photo-Optical Instrumentation Engineers (SPIE) Conference Series, Vol. 8444, Ground-based and Airborne Telescopes IV, ed. L. M. Stepp, R. Gilmozzi, & H. J. Hall, 844403, doi: [10.1117/12.925494](https://doi.org/10.1117/12.925494)
- Hollweg, J. V. 1978, SoPh, 56, 305, doi: [10.1007/BF00152474](https://doi.org/10.1007/BF00152474)
- Howard, R. A., Vourlidas, A., & Stenborg, G. 2023, Frontiers in Astronomy and Space Sciences, 10, 1264226, doi: [10.3389/fspas.2023.1264226](https://doi.org/10.3389/fspas.2023.1264226)
- Jess, D. B., Pascoe, D. J., Christian, D. J., et al. 2012, ApJL, 744, L5, doi: [10.1088/2041-8205/744/1/L5](https://doi.org/10.1088/2041-8205/744/1/L5)
- Johnston, Z., Squire, J., Mallet, A., & Meyrand, R. 2022, Physics of Plasmas, 29, 072902, doi: [10.1063/5.0097983](https://doi.org/10.1063/5.0097983)
- Kalkofen, W. 1997, ApJL, 486, L145, doi: [10.1086/310842](https://doi.org/10.1086/310842)
- Kasper, J. C., Bale, S. D., Belcher, J. W., et al. 2019, Nature, 576, 228, doi: [10.1038/s41586-019-1813-z](https://doi.org/10.1038/s41586-019-1813-z)
- Krasnoselskikh, V., Larosa, A., Agapitov, O., et al. 2020, ApJ, 893, 93, doi: [10.3847/1538-4357/ab7f2d](https://doi.org/10.3847/1538-4357/ab7f2d)
- Laker, R., Horbury, T. S., Bale, S. D., et al. 2021, A&A, 650, A1, doi: [10.1051/0004-6361/202039354](https://doi.org/10.1051/0004-6361/202039354)
- Larosa, A., Chen, C. H. K., McIntyre, J. R., Jagarlamudi, V. K., & Sorriso-Valvo, L. 2024, A&A, 686, A238, doi: [10.1051/0004-6361/202450030](https://doi.org/10.1051/0004-6361/202450030)
- Larosa, A., Krasnoselskikh, V., Dudok de Wit, T., et al. 2021, A&A, 650, A3, doi: [10.1051/0004-6361/202039442](https://doi.org/10.1051/0004-6361/202039442)
- Lee, J. 2022, Reviews of Modern Plasma Physics, 6, 32, doi: [10.1007/s41614-022-00096-y](https://doi.org/10.1007/s41614-022-00096-y)
- Lee, J., Wang, H., Wang, J., & Wang, M. 2024, ApJ, 963, 79, doi: [10.3847/1538-4357/ad23e0](https://doi.org/10.3847/1538-4357/ad23e0)
- Lee, J., Yurchyshyn, V., Wang, H., et al. 2022, ApJL, 935, L27, doi: [10.3847/2041-8213/ac86bf](https://doi.org/10.3847/2041-8213/ac86bf)
- Mackenzie Dover, F., Sharma, R., & Erdélyi, R. 2021, ApJ, 913, 19, doi: [10.3847/1538-4357/abefd1](https://doi.org/10.3847/1538-4357/abefd1)
- . 2022, ApJ, 929, 88, doi: [10.3847/1538-4357/ac5aa9](https://doi.org/10.3847/1538-4357/ac5aa9)
- Mallet, A., Squire, J., Chandran, B. D. G., Bowen, T., & Bale, S. D. 2021, ApJ, 918, 62, doi: [10.3847/1538-4357/ac0c12](https://doi.org/10.3847/1538-4357/ac0c12)
- Nisenson, P., van Ballegooijen, A. A., de Wijn, A. G., & Sütterlin, P. 2003, ApJ, 587, 458, doi: [10.1086/368067](https://doi.org/10.1086/368067)
- Okamoto, T. J., & De Pontieu, B. 2011, ApJL, 736, L24, doi: [10.1088/2041-8205/736/2/L24](https://doi.org/10.1088/2041-8205/736/2/L24)
- Parker, E. N. 1958, ApJ, 128, 664, doi: [10.1086/146579](https://doi.org/10.1086/146579)
- . 1965, SSRv, 4, 666, doi: [10.1007/BF00216273](https://doi.org/10.1007/BF00216273)
- Parnell, C. E. 2002, MNRAS, 335, 389, doi: [10.1046/j.1365-8711.2002.05618.x](https://doi.org/10.1046/j.1365-8711.2002.05618.x)
- Parnell, C. E., DeForest, C. E., Hagenaar, H. J., et al. 2009, ApJ, 698, 75, doi: [10.1088/0004-637X/698/1/75](https://doi.org/10.1088/0004-637X/698/1/75)
- Raouafi, N. E., Stenborg, G., Seaton, D. B., et al. 2023a, ApJ, 945, 28, doi: [10.3847/1538-4357/acaf6c](https://doi.org/10.3847/1538-4357/acaf6c)
- Raouafi, N. E., Matteini, L., Squire, J., et al. 2023b, SSRv, 219, 8, doi: [10.1007/s11214-023-00952-4](https://doi.org/10.1007/s11214-023-00952-4)
- Rivera, Y. J., Badman, S. T., Stevens, M. L., et al. 2024, Science, 385, 962, doi: [10.1126/science.adk6953](https://doi.org/10.1126/science.adk6953)
- Schwartz, S. J., & Bel, N. 1984, A&A, 137, 128
- Secchi, A. 1877, L'astronomia in Roma nel pontificato DI Pio IX.
- Sharma, R., & Morton, R. J. 2023, Nature Astronomy, 7, 1301, doi: [10.1038/s41550-023-02070-1](https://doi.org/10.1038/s41550-023-02070-1)

- Shi, C., Panasenco, O., Velli, M., et al. 2022, *ApJ*, 934, 152, doi: [10.3847/1538-4357/ac7c11](https://doi.org/10.3847/1538-4357/ac7c11)
- Shoda, M., Chandran, B. D. G., & Cranmer, S. R. 2021, *ApJ*, 915, 52, doi: [10.3847/1538-4357/abfdbc](https://doi.org/10.3847/1538-4357/abfdbc)
- Simon, G. W., & Leighton, R. B. 1964, *ApJ*, 140, 1120, doi: [10.1086/148010](https://doi.org/10.1086/148010)
- Soler, R., Terradas, J., Oliver, R., & Ballester, J. L. 2019, *ApJ*, 871, 3, doi: [10.3847/1538-4357/aaf64c](https://doi.org/10.3847/1538-4357/aaf64c)
- Squire, J., Chandran, B. D. G., & Meyrand, R. 2020, *ApJL*, 891, L2, doi: [10.3847/2041-8213/ab74e1](https://doi.org/10.3847/2041-8213/ab74e1)
- Squire, J., Johnston, Z., Mallet, A., & Meyrand, R. 2022, *Physics of Plasmas*, 29, 112903, doi: [10.1063/5.0099924](https://doi.org/10.1063/5.0099924)
- Stix, M. 2004, *The Sun: An Introduction*
- Touresse, J., Pariat, E., Froment, C., et al. 2024, *A&A*, 692, A71, doi: [10.1051/0004-6361/202452019](https://doi.org/10.1051/0004-6361/202452019)
- Ulmschneider, P., Zaehring, K., & Musielak, Z. E. 1991, *A&A*, 241, 625
- Utz, D., Hanslmeier, A., Muller, R., et al. 2010, *A&A*, 511, A39, doi: [10.1051/0004-6361/200913085](https://doi.org/10.1051/0004-6361/200913085)
- van Ballegooijen, A. A., Nisenson, P., Noyes, R. W., et al. 1998, *ApJ*, 509, 435, doi: [10.1086/306471](https://doi.org/10.1086/306471)
- Verscharen, D., Klein, K. G., & Maruca, B. A. 2019, *Living Reviews in Solar Physics*, 16, 5, doi: [10.1007/s41116-019-0021-0](https://doi.org/10.1007/s41116-019-0021-0)
- Viall, N. M., DeForest, C. E., & Kepko, L. 2021, *Frontiers in Astronomy and Space Sciences*, 8, 139, doi: [10.3389/fspas.2021.735034](https://doi.org/10.3389/fspas.2021.735034)
- Wang, Y. M., & Sheeley, N. R., Jr. 1990, *ApJ*, 355, 726, doi: [10.1086/168805](https://doi.org/10.1086/168805)
- Wedemeyer-Böhm, S., Scullion, E., Steiner, O., et al. 2012, *Nature*, 486, 505, doi: [10.1038/nature11202](https://doi.org/10.1038/nature11202)
- Wyper, P. F., Pariat, E., Squire, J., Touresse, J., & Matteini, L. 2024, in *AGU Fall Meeting Abstracts*, Vol. 2024, SH24A-01
- Zhugzhda, I. D., & Locans, V. 1982, *SoPh*, 76, 77, doi: [10.1007/BF00214131](https://doi.org/10.1007/BF00214131)
- Zirin, H. 1988, *Astrophysics of the sun*